Report on the Implementation of the Homogeneous Nucleation Scheme in MARMOT-based Phase Field Simulations

Fuel Cycle Research & Development

Prepared for
U.S. Department of Energy
Fuel Cycle R&D Program

Yulan Li, Shenyang Hu, Xin Sun
Pacific Northwest National Laboratory, Richland, WA 99352

M2MS-13PN0602054
PNNL-22829

Reviewed by:

National Technical Director, Nuclear Energy
Advanced Modeling and Simulation

Keith Bradley Date

Concurred by:

Acting Director, Advanced Modeling and
Simulation Office

Trevor Cook Date

Approved by:

Deputy Assistant Secretary, Nuclear Energy

Shane Johnson Date

Report on the Implementation of the Homogeneous Nucleation Scheme in MARMOT-based Phase Field Simulations

SUMMARY

In this report, we summarize our effort in developing mesoscale phase field (PF) models for predicting precipitation kinetics in alloys during thermal aging and/or under irradiation in nuclear reactors. The first part focuses on developing a method to predict the thermodynamic properties of critical nuclei, such as the sizes and concentration profiles of critical nuclei, and the nucleation barrier. These properties are crucial for quantitative simulations of precipitate evolution kinetics with PF models. An iron-chromium (Fe-Cr) alloy is chosen as a model alloy because it has valid thermodynamic and kinetic data and is an important structural material in nuclear reactors. A constrained shrinking dimer dynamics method is developed to search for the energy minimum path during nucleation. With the method, we are able to predict the concentration profiles of the critical nuclei of Cr-rich precipitates and nucleation energy barriers. Simulations show that Cr concentration distribution in the critical nucleus strongly depends on the overall Cr concentration and temperature. The Cr concentration inside the critical nucleus is much smaller than the equilibrium concentration calculated by the equilibrium phase diagram. This implies that a non-classical nucleation theory should be used to deal with the nucleation of Cr precipitates in Fe-Cr alloys. The growth kinetics of both classical and non-classical nuclei is investigated using the PF approach. A number of interesting phenomena are observed from the simulations: 1) a critical classical nucleus first shrinks toward its non-classical nucleus, then grows; 2) a non-classical nucleus has much slower growth kinetics at its earlier growth stage compared to the diffusion-controlled growth kinetics; 3) a critical classical nucleus grows faster at the earlier growth stage than the non-classical nucleus. All of these results demonstrate that it is critical to introduce the correct critical nuclei into PF modeling to correctly capture the kinetics of precipitation.

In most alloys, the matrix phase and precipitate phase have different concentrations and crystal structures. For example, copper (Cu) precipitates in Fe-Cu alloys have a face-centered cubic (fcc) crystal structure, while the matrix Fe-Cu solid solution has a body-centered cubic (bcc) structure at low temperature. The Wheeler-Boettinger-McFadden (WBM) and Kim-Kim-Suzuki (KKS) models, where both concentrations and order parameters are chosen to describe the microstructures, are commonly used to model precipitations in these alloys. The WBM and KKS models have yet to be implemented into MARMOT. In the second part of this report, we focus on implementing the WBM and KKS models into MARMOT. The Fe-Cu alloys, which are important structure materials in nuclear reactors, are used as the model alloys to test the models.

Key words: precipitation; non-classical nucleation; Fe alloys; phase field modeling; MARMOT.

CONTENTS

FIGURES

TABLES

ACRONYMS

1-D	one-dimensional (one dimensions)
2-D	two-dimensional (two dimensions)
3-D	three-dimensional (three dimensions)
bcc	body-centered cubic
CSDD	constrained shrinking dimer dynamics
fcc	face-centered cubic
Fe-Cr	iron-chromium
Fe-Cu	iron-copper
H	hour(s)
J/m^2	joule per square meter
K	Kelvin
kMC	kinetic Monte Carlo
KKS	Kim-Kim-Suzuki
MOOSE	Multiphysics Object-Oriented Simulation Environment
PDE	partial differential equation(s)
PF	phase field
PNNL	Pacific Northwest National Laboratory
TAP	tomographic atom probe
WBM	Wheeler-Boettinger-McFadden

FUEL CYCLE R&D PROGRAM

REPORT ON THE IMPLEMENTATION OF THE HOMOGENEOUS NUCLEATION SCHEME IN MARMOT-BASED PHASE FIELD SIMULATION

1. Introduction

Nucleation is a ubiquitous physical phenomenon. It occurs when a material becomes metastable with respect to its transformation to a new state or phase. For example, the formation of liquid droplets in saturated vapor is a nucleation process. Typically, nucleation is divided into two types, i.e., homogeneous and heterogeneous nucleation. Heterogeneous nucleation happens preferentially on surfaces, pre-existing interfaces (grain boundaries), dislocations or impurities, etc. Nucleation without preferential nucleation sites is homogeneous nucleation. Homogeneous nucleation occurs spontaneously and randomly, but it requires supersaturation, superheating, or supercooling of the medium. Compared to heterogeneous nucleation, homogeneous nucleation occurs with much more difficulty in the interior of a uniform substance.

Computer simulations of homogeneous nucleation are an extraordinary difficult issue. In a previous report, we propose a scheme to deal with homogeneous nucleation by introducing classical nuclei into a phase field (PF) simulation cell.[1] Actually, the critical nuclei are not always of the classical profile, i.e., having bulk properties. Both kinetic Monte Carlo (kMC) simulations[2] and tomographic atom probe (TAP) experiments[3] show that the concentration inside small chromium (Cr) precipitates in iron-chromium (Fe-Cr) alloys is smaller than the equilibrium concentration, and it increases with precipitate growth. This implies that the nucleation of Cr precipitates is non-classical. In this report, one objective is to develop a method to predict the thermodynamic properties of non-classical critical nuclei, including concentration profiles inside the critical nuclei and nucleation energy barrier. These thermodynamic properties are input parameters for introducing nuclei into PF simulation cells.

MARMOT is a PF-method-based multiphysics simulation tool at the mesoscale. It is implemented using the Multiphysics Object-oriented Simulation Environment (MOOSE)

framework, a massively parallel, finite element-based system to solve large systems of equations using the Jacobian-free Newton Krylov (JFNK) method.[4] The main governing equations for PF modeling are Cahn-Hilliard equations (the fourth-order partial differential equations (PDE)) and Allen-Cahn equations (the second-order PDEs)[5]. The implementation of pure Cahn-Hilliard and pure Allen-Cahn equations into MARMOT and their applications have been reported by Tonks et al.[6] However, in most alloys, the matrix and precipitate phases have different concentrations and crystal structures. For example, copper (Cu) precipitates in Fe-Cu alloys have a face-centered cubic (fcc) crystal structure, while the matrix (i.e., Fe-Cu solid solution) has a body-centered cubic (bcc) structure at low temperature. PF models, such as the Wheeler-Boettinger-McFadden (WBM) model[2] and an equivalent model developed by Kim et al.[7] (referred to as "KKS" model herein), are commonly used to model precipitation in such alloys. Both must solve coevolution of concentrations and order parameters governed by Cahn-Hilliard equations and Allen-Cahn equations, respectively. The WBM model and KKS models have yet to be implemented into MARMOT. Another objective of this report is to implement the WBM and KKS models into MARMOT.

This report is organized into two main sections and a conclusion. In the first section, an efficient constrained shrinking dimer dynamics (CSDD) method[8] is proposed to search for the energy minimum path during the nucleation of precipitates. With the method and valid thermodynamic properties of Fe-Cr alloys, we are able to systematically investigate the effect of temperatures and overall Cr concentrations on the thermodynamic properties of critical nuclei in Fe-Cr alloys. The growth kinetics of Cr nuclei with predicted concentration profiles inside the critical nucleus are examined using the PF approach. In the second section, both the WBM and KKS models are used to describe the precipitation kinetics of fcc Cu precipitates in a bcc Fe-Cu matrix and are implemented into MARMOT. Finally, we offer our concluding remarks.

2. Non-classical critical nuclei and their growth kinetics of Cr precipitation in Fe-Cr alloys

In fusion and advanced fission reactor components, high-chromium ferritic/martensitic steels are the preferred candidates for structural materials.[9] The addition of Cr has a positive effect on mechanical, corrosion, and radiation resistance properties. However, it is well known that Fe-Cr alloys undergo thermal- and irradiation-induced phase separation from the solid solution into Fe-

rich and Cr-rich phases in the temperature range spanning 300°C~550°C.[10, 11] The phase separation causes material property degradation, such as embrittlement and stress corrosion cracking.[10, 12] In predicting microstructure evolution and material property degradation, a fundamental understanding of the thermodynamics, mechanisms, and kinetics of phase separation is of significant technological importance.

Phase separation in Fe-Cr solid solutions happens via two different mechanisms: 1) spinodal decomposition and 2) Cr-rich phase nucleation and growth. Cr concentration and aging temperature dictate which mechanism operates. Spinodal decomposition can be naturally simulated using atomistic and field theoretical methods by introducing any fluctuations of temperature, composition, and/or order parameters. However, modeling nucleation generally is considered one of the most challenging issues. For example, the PF approach is a powerful simulation tool to predict microstructure evolution during phase separation.[5] Although the PF approach accounts for energy changes during nucleation, such as a bulk free energy decrease that is proportional to the nucleus volume, an interfacial energy increase that is proportional to the interfacial area, or long-range interaction energies (e.g., elastic energy), it is unable to simulate the nucleation process because the PF approach assumes that microstructure evolution is driven by the energy minimization while nucleation needs to overcome an energy barrier. Therefore, to simulate the phase separation, PF simulations must introduce critical nuclei into the simulation cells. According to classical nucleation theory, the thermodynamic and kinetic information, including the critical nucleus radius, nucleation barrier, and nucleation rate, can be calculated once the chemical free energy, interfacial energy, and long-range interaction energy are known. However, experiments[3] and kMC simulations[2] all show that the nucleation of Cr precipitates in Fe-Cr alloys is a non-classical nucleation, i.e., the Cr concentration inside the nucleus is not the same as the thermal equilibrium concentration, particularly when the Fe-Cr alloys have high supersaturations. The thermodynamic and kinetic information of non-classical nuclei in Fe-Cr alloys are lacking for the PF simulations. Furthermore, it is unknown how the critical nuclei from non-classical nucleation and classical nucleation affect growth kinetics.

In Fe-Cr alloys, Cr precipitates are Cr-rich phases with the same structure of the matrix phase (i.e., bcc Fe-Cr solid solution). Therefore, the precipitate microstructure in bcc Fe-Cr alloys can be uniquely described by Cr concentration. In a PF approach framework, the concentration of Cr,

$C_{Cr}(\mathbf{r},t)$, is employed as the PF variable, where $\mathbf{r}=(r_1, r_2, r_3)$ is the spatial coordinate and t is time. Compared with Cr solubility in Fe-Cr alloys, thermal equilibrium vacancy concentration is very small and, thus, ignored in the present model. So, the concentration of Fe is 1-C_{Cr}. Due to the low lattice mismatch, the elastic energy contribution in the Fe-Cr system is negligible and omitted in this study. Therefore, the total free energy of the binary system can be expressed as:

$$E(C_{Cr},T)=\int_V\left[\frac{NA_0}{\Omega_0}f(C_{Cr},T)+\frac{\kappa}{2}\left|\nabla C_{Cr}\right|^2\right]dV\,, \tag{1}$$

where $\nabla=\left(\partial/\partial r_1+\partial/\partial r_2+\partial/\partial r_3\right)$ is the gradient operator and V is the volume of the considered system. $N=6.022\times10^{23}$ [atom/mol] is the Avogadro's constant. $\Omega_0=1.4087\times10^{-5}$ [m^3/mol] is the molar volume of bcc Fe, constant $A_0=1.602\times10^{-19}$ [J/eV]. $f(C_{Cr},T)$ is the chemical free energy density per atom in electron voltage (eV), and κ is the interfacial energy coefficient.

Because the concentration C_{Cr} is a conserved field variable, its temporal evolution is described by the Cahn-Hillard equation:

$$\frac{\partial C_{Cr}}{\partial t}=-\nabla\cdot\left(-M\nabla\frac{\delta E}{\delta C_{Cr}}\right)=\nabla\cdot M\nabla\left[\frac{NA_0}{\Omega_0}\frac{\partial f}{\partial C_{Cr}}-\kappa\nabla^2C_{Cr}\right], \tag{2}$$

where M is the mobility of C_{Cr} and related to Cr atom diffusivity, D, as $M=D\Omega_0/(\Re T)$ with $\Re$ being the gas constant of $\Re=8.314\,\mathrm{J/(mol\cdot K)}$. For numerically solving Eq. (2), the following normalizations are used: $t^*=\frac{t}{t_0}$, $t_0=\frac{l_0^2\Omega_0}{NA_0M}$, $r_i^*=\frac{r_i}{l_0}$, $\kappa^*=\frac{\kappa\Omega_0}{NA_0l_0^2}$, and $\nabla=\left(\frac{\partial}{\partial r_1},\frac{\partial}{\partial r_2},\frac{\partial}{\partial r_3}\right)$ $=\frac{1}{l_0}\left(\frac{\partial}{\partial r_1^*},\frac{\partial}{\partial r_2^*},\frac{\partial}{\partial r_3^*}\right)=\frac{1}{l_0}\nabla^*$. l_0 is a characteristic length. Therefore, Eq. (2) is rewritten as:

$$\frac{\partial C_{Cr}}{\partial t^*}=\nabla^{*2}\left[\frac{\partial f}{\partial C_{Cr}}-\kappa^*\nabla^{*2}C_{Cr}\right]. \tag{3}$$

Equation (3) will be solved numerically using the semi-implicit Fourier-spectral method[13] under periodic boundary conditions.

2.1 Assessment of thermodynamic properties

2.1.1 Chemical free energy

To predict Cr precipitate formation and growth or solve the evolution equation (3), the free energy density $f(C_{Cr},T)$ is needed. As a result of many people's valuable efforts, an analytical free energy density now is available for the Fe-Cr system:[14, 15]

$$f(C_{Cr},T)=G(1-C_{Cr},T) \tag{4}$$

$$\begin{aligned} G(x,T)=G_0(x,T)\frac{T}{T_0}+H_a(x)-H_b(x)T\log T-H_c(x)T^2+H_d(x)\frac{T^3}{2} \\ +H_e(x)T+k_BT\left[x\log x+(1-x)\log(1-x)\right], \end{aligned} \tag{5}$$

$$H_a(x)=x(1-x)\sum_{i=0}^{5}a_i(1-2x)^i+a_6x+a_7(1-x), \tag{6}$$

$$H_{\xi\in\{b,c,d\}}(x)=\sum_{i=0}^{3}\xi_i(1-x)^i, \tag{7}$$

$$H_e(x)=-\frac{H_a(x)}{T_0}+H_b(x)\log T_0+H_c(x)T_0+H_d(x)\frac{T_0^2}{2}, \tag{8}$$

$$G_0(x)=x(1-x)\sum_{i=0}^{5}f_i(1-2x)^i+f_6x+f_7(1-x), \tag{9}$$

where T_0=410 K, k_B=8.617310^{-5} eV/K is the Boltzmann constant, and $x=1-C_{Cr}$ is the concentration of Fe. Table I lists the corresponding coefficients. At the given temperatures, the free energies are plotted in Figure 1.

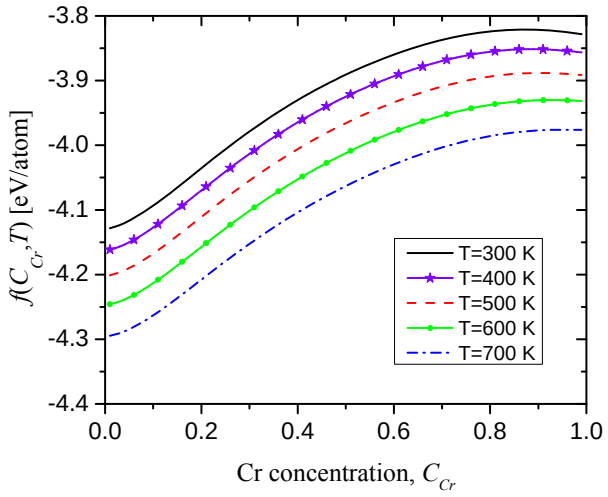

Figure 1. Chemical free energy of Fe-Cr alloys.

Table I: Coefficients for the Fe-Cr free energy given in Eqs. (4-9).

ξ	A	B	c	d	f
ξ_0	0.3856	2.630×10^{-4}	3.145×10^{-9}	-1.7601×10^{-13}	0.3817
ξ_1	0.0973	4.696×10^{-5}	-2.203×10^{-8}	5.579×10^{-12}	0.1007
ξ_2	-0.0467	-4.959×10^{-5}	3.960×10^{-8}	-5.935×10^{-12}	-0.0485
ξ_3	0.1945	1.133×10^{-5}	-3.090×10^{-8}	1.229×10^{-11}	0.1541
ξ_4	-0.1856				-0.1684
ξ_5	0.0044				0.0416
ξ_6	-4.1231				-4.1671
ξ_7	-3.8366				-3.8602

With the free energy density $f(C_{Cr},T)$, we calculate the Cr solubility, spinodal concentrations, and equilibrium concentration of Cr precipitate in the Fe-Cr alloys at different temperatures. The chemical free energy $f(C_{Cr},T)$ has a common tangent at the Cr solubility in Fe-Cr solid solution and Cr equilibrium concentration in Cr precipitate. The spinodal concentration is associated with the inflection point of $f(C_{Cr},T)$. Table II lists the Cr solubility and spinodal concentrations in Fe-rich side and Cr thermodynamic equilibrium concentration in Cr precipitates.

Table II. Cr solubility and spinodal concentrations in Fe-rich side and Cr equilibrium concentration in Cr precipitates.

Temperature (K)	Cr solubility ($C_{Cr}^{M,eq}$)	Cr spinodal concentration	Cr equilibrium concentration in Cr precipitate ($C_{Cr}^{P,eq}$)
300	0.04199	0.19049	1.0
400	0.04829	0.19422	1.0
500	0.05501	0.19840	0.99998
600	0.06223	0.20309	0.99989
700	0.07008	0.20840	0.99958

2.1.2 Interfacial energy

In the PF model described in Eqs. (1) and (2), both the chemical free energy $f(C_{Cr},T)$ and the gradient energy contribute to the interfacial energy. For given characteristic length l_0 and gradient coefficient κ, the interfacial energy of a flat interface can be numerically calculated. To do so, we place a precipitate at the center of a one-dimensional (1-D) simulation cell ($512\,l_0 \times l_0 \times l_0$) and allow the system to approach equilibrium through Cr diffusion. At the equilibrium state, the equilibrium concentrations in both precipitate and matrix and the equilibrium interface concentration profile reach. Then, interfacial energy can be numerically calculated with the equilibrium concentration profile by:

$$\gamma = \frac{1}{2}\frac{NA_0}{\Omega_0}\int_V \left[f(C_{Cr},T) + \frac{1}{2}\kappa^* \left| \nabla^* C_{Cr} \right|^2 \right] dV \,, \tag{10}$$

where the ½ factor outside the integral is due to the fact that there are two interfaces in the 1-D model. By tailoring the characteristic length l_0 and gradient coefficient κ^*, the PF model can correctly describe the interfacial energy of Cr precipitates. In general cases, the interfacial energy is anisotropic. Then, the gradient coefficient κ is a tensor. The same method can be used to determine the tensor κ.

By taking l_0 as the α-Fe lattice parameter, i.e., $l_0 = 0.287\,\text{nm}$ and $\kappa^* = 0.8$, the corresponding interface energies are calculated with Eq. (10) for different temperatures. They are listed in Table III and compared with those obtained by Schwen et al.[14] through fitting the results

from Sadigh and Erhart.[16] It is evident that the interfacial energy from this work is slightly larger than that from the previous works. This can be adjusted by taking a smaller l_0. Figure 2 provides the corresponding equilibrium profiles for an average concentration of C_{Cr}=0.158% at different temperatures. From the figure's inset, we can see the PF model can aptly predict the equilibrium concentrations.

Table III. Interfacial energies at different temperatures.

Temperature (K)	This work with $\kappa^* = 0.8$ $l_0 = 0.287\,\text{nm}$ (J/m^2)	Work [14, 16] (J/m^2)
300	0.5334	0.4049
400	0.5016	0.3910
500	0.4811	0.3762
600	0.4382	0.3606
700	0.4093	0.3441

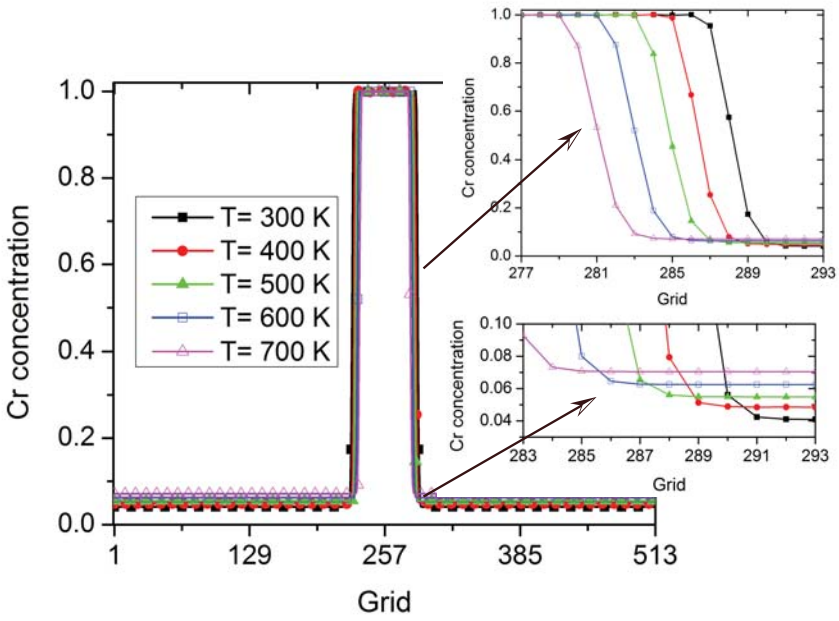

Figure 2. Equilibrium profiles of Cr precipitates in a 1-D simulation model when Cr average concentration is c_0=0.158%. The two insets display the Cr concentration at the interface and matrix phases, respectively.

2.2 Constrained Shrinking Dimer Dynamics

In recent years, high-performance numerical methods have been proposed to find the critical nucleus[17, 18] and have been applied to nucleation in solid-state phase transformation.[8, 19] In particular, shrinking dimer dynamics (SDD)[20] and its extension on a constrained manifold, or CSDD,[21] have been used successfully to efficiently compute the saddle point associated with an energy functional. Here, we apply the CSDD to predict the critical nuclei of Cr precipitates in Fe-Cr alloys based on the free energy and interfacial energy provided in the previous section. The constraint of the current model is from the mass conservation, i.e.,

$$G(C_{Cr}) = \int_V [C_{Cr}(\mathbf{r},T) - c_0]dV = 0. \tag{11}$$

To construct the dimer system, we let $C_{Cr(1)}$ and $C_{Cr(2)}$ be the two end points of a dimer with a length of $l = |C_{Cr(1)} - C_{Cr(2)}|$. The dimer orientation is given by a unit vector v so $C_{Cr(1)} - C_{Cr(2)} = lv$. The rotation center of a dimer is defined as $C_{Cr}^{\alpha} = (1-\alpha)C_{Cr(1)} + \alpha C_{Cr(2)}$, where the parameter $\alpha \in [0,1]$. Thus, the geometric center (midpoint of the dimer) corresponds to $\alpha = 0.5$. Thereby, $C_{Cr(1)} = C_{Cr}^{\alpha} + \alpha lv$, $C_{Cr(2)} = C_{Cr}^{\alpha} - (1-\alpha)lv$.

To enforce the constraint, CSDD uses the projected natural force, which is the negative gradient force projected on the tangential hyperplane of the constraint, i.e.,

$$\tilde{F}(C_{Cr}) = \frac{\delta E^*(C_{Cr})}{\delta C_{Cr}} - \frac{1}{V}\int_V \frac{\delta E^*(C_{Cr})}{\delta C_{Cr}} dV = \left(\frac{\partial f}{\partial C_{Cr}} - \kappa^* \nabla^{*2} C_{Cr}\right) - \frac{1}{V}\int_V \left(\frac{\partial f}{\partial C_{Cr}} - \kappa^* \nabla^{*2} C_{Cr}\right) dV, \tag{12}$$

with $E^*(C_{Cr}) = \frac{\Omega_0}{NA_0} E(C_{Cr}) = \int_V \left[f(C_{Cr},T) + \frac{\kappa^*}{2} |\nabla^* C_{Cr}|^2 \right] dV$. Following the SDD, the formulation of the CSDD is given by:[21]

$$\begin{cases} \mu_1 \dfrac{\partial C_{Cr}^{\alpha}}{\partial t} = \left(I - 2vv^T\right)\left[(1-\alpha)\tilde{F}_1 + \alpha \tilde{F}_2\right], \\ \mu_2 \dfrac{\partial v}{\partial t} = \left(I - vv^T\right)\dfrac{\left(\tilde{F}_1 - \tilde{F}_2\right)}{l}, \\ \mu_3 \dfrac{dl}{dt} = -\dfrac{dE_{\text{dimer}}(l)}{dl}, \end{cases} \tag{13}$$

with the relaxation constants μ_1, μ_2, and μ_3. Also, $\widetilde{F}_1 = \widetilde{F}\left(C_{Cr(1)}\right)$ and $\widetilde{F}_2 = \widetilde{F}\left(C_{Cr(2)}\right)$. The first equation of the CSDD in Eq. (13) represents the translation step of the dimer, and the operator $\left(I - 2vv^T\right)$ is the Householder mirror reflection, which reverses the component of the negative gradient force at v direction. The rotation step of the CSDD is the second equation in Eq. (13). The third equation in Eq. (13) follows a gradient flow of the dimer energy, resulting in the dimer shrinking over time and the solution of Eq. (13) converging to an exact saddle point. In this work, we choose an auxiliary function $E_{\text{dimer}}(l) = l^2/2$, which provides an exponential decay of the dimer length.

The initial condition of the CSDD must satisfy the following compatibility assumption: $G\left(C_{Cr}^0\right) = 0$, $|v_0(\mathbf{r})| = 1$, $\int_V v_0(\mathbf{r})dV = 0$. The $|v_0|$ represents the magnitude of vector v_0. One straightforward way to implement time discretization of the CSDD, is to apply the modified forward Euler scheme:

$$\begin{cases} C_{Cr}^{\alpha,n+1} = C_{Cr}^{\alpha,n} + \dfrac{\Delta t}{\mu_1}\left(I - 2v^n\left(v^n\right)^T\right)\left[(1-\alpha)\widetilde{F}\left(C_{Cr(1)}^n\right) + \alpha\widetilde{F}\left(C_{Cr(2)}^n\right)\right], \\ \bar{v}^{n+1} = v^n + \dfrac{\Delta t\left[\widetilde{F}\left(C_{Cr(1)}^n\right) - \widetilde{F}\left(C_{Cr(2)}^n\right)\right]}{\mu_2 l^n}, v^{n+1} = \dfrac{\bar{v}^{n+1}}{\left\|\bar{v}^{n+1}\right\|}, \\ l^{n+1} = \dfrac{l^n}{1 + \Delta t/\mu_3}, \end{cases} \tag{14}$$

which performs a normalization on v at each iteration for the dimer rotation step so the scheme improves the local stability and optimal error reduction rate. To further improve the Euler method's stability and afford a larger time step in the algorithm, we employ a semi-implicit splitting scheme for the CSDD, where the principal linear operator is treated implicitly to reduce the associated stability constraint while the nonlinear terms still are treated explicitly to avoid the expensive process of solving nonlinear equations at each time step. To achieve exponential convergence in space, the Fourier-spectral method is used for spatial discretization. In our calculations, $\mu_1 = \mu_2 = \mu_3 = 1$ and $\alpha = 0.5$.

2.3 Non-classical critical nuclei and nucleation barriers of Cr precipitates in Fe-Cr alloys

Here, we assume that interfacial energy is isotropic. Thus, the critical nucleus will be a sphere in a real three-dimensional (3-D) space. Experiments[3] also show that Cr precipitates in Fe-Cr alloys have spherical shapes. As the chemical free energy of Eq. (4) depends on Cr concentration and temperature, the critical nucleus profile also will vary with overall Cr concentration and temperature. To calculate the concentration profiles of critical nuclei, we consider a 3-D simulation cell of $64\,l_0 \times 64\,l_0 \times 64\,l_0$. For a given temperature (T) and Cr overall concentration (c_0), the critical nucleus profile is obtained by solving the CSDD equations. Figure 3 plots critical nuclei profile dependence on Cr overall concentration (c_0) and temperature (T). We can see that the concentrations inside the nuclei are much smaller than the equilibrium concentration of Cr-precipitates (i.e., $C_{Cr}^{P,eq} \approx 1$) calculated from the equilibrium phase diagram. Experiments from atom probe observations[3] also demonstrate that the Cr-concentration in the nuclei does not have to be its bulk equilibrium values. Therefore, the critical nucleus of Cr precipitate is non-classical. Although it is difficult to define the critical size of a nucleus, we can clearly see that Cr content inside the nuclei increases with a decrease of the Cr overall concentration and an increase in temperature.

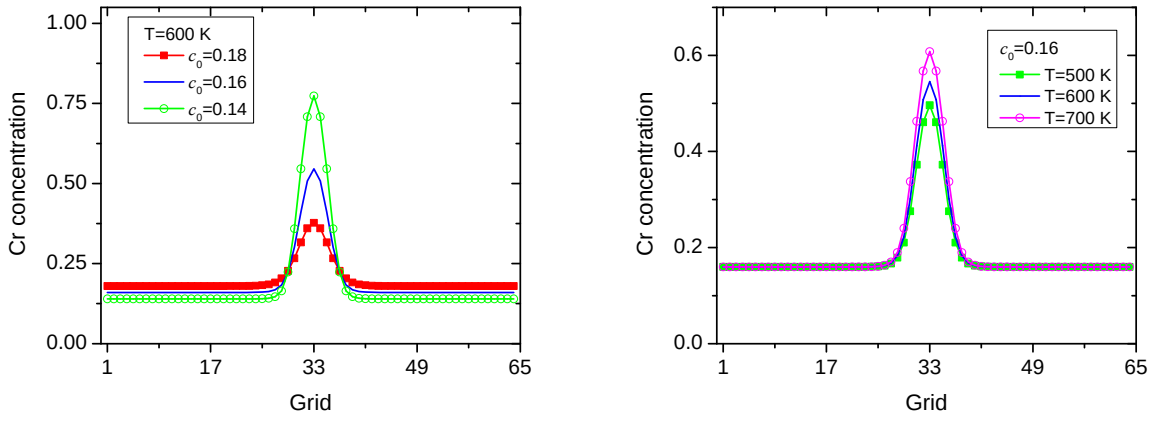

(a) (b)

Figure 3. Cr nucleus profiles at (a) different temperature (T) and (b) different Cr overall concentration (c_0). The plots illustrate the Cr concentration distribution along the diameter of the spherical nuclei.

To validate that the concentration profiles predicted from the CSDD are critical profiles, we numerically examine the evolution of the nucleus. Figure 4(a) displays the profiles of the critical nuclei for c_0=0.16 at T=500 K and T=501 K, respectively. The nucleus at T=501 K is slightly larger than the one at T=500 K. However, the difference between them is barely identified in the figure. By introducing the nuclei into the PF simulation cells, respectively, and evolving the PF equation (Eq. (3)) at the corresponding temperatures, Figure 4(b) and Figure 4(c) indicate that both nuclei are stable and grow. If the slightly small nucleus obtained at T=500 K is used for T=501K, the nucleus becomes unstable and shrinks as shown in Figure 4(d). These results numerically demonstrate that the CSDD method can provide the critical nucleus concentration profiles.

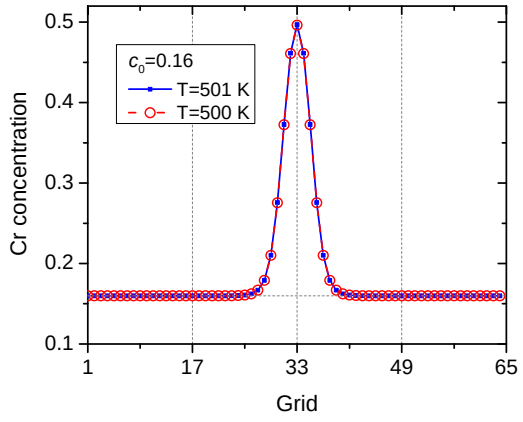

(a)

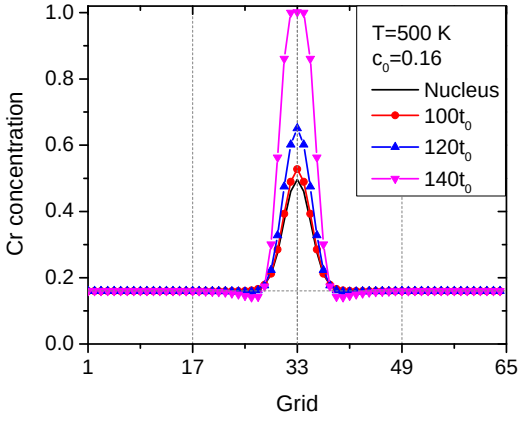

(b)

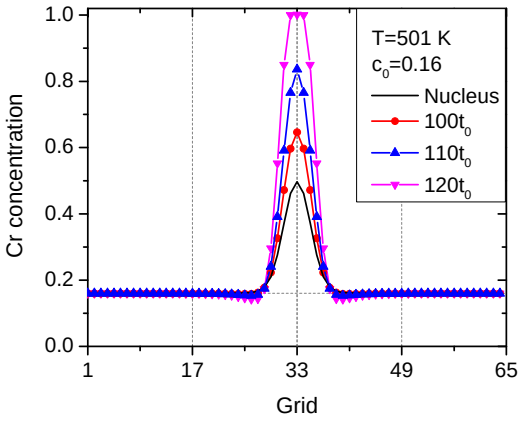

(c)

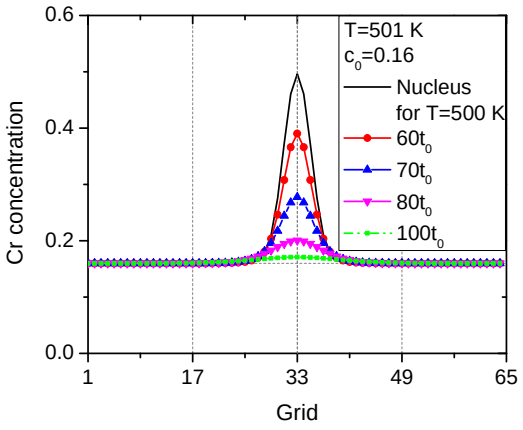

(d)

Figure 4. Critical nucleus concentration profiles for c_0=0.16 at T=500 K and 501 K and their temporal evolution. (a) Critical profile. (b) Evolution of the nucleus of T=500 K at T=500 K. (c) Evolution of the nucleus of T=501 K at T=501 K. (d) Evolution of T=500 K nucleus at T=501 K.

It is known that the critical nucleus is associated with the concentration fluctuation that has the minimum free energy increase among all fluctuations, leading to growth. In the following, we calculate the energy excess, the energy difference between the system with a critical nucleus, and the original supersaturated system with uniform concentration:

$$E_{excess} = F \Big/ \left(\frac{l_0^3 N A_0}{\Omega_0} \right) = \int_{V^*} \left[f(C_{Cr}, T) + \frac{1}{2}\kappa^* \left| \nabla^* C_{Cr} \right|^2 - f(c_0, T) \right] dV^* . \quad (15)$$

Actually, E_{excess} is the nucleation energy barrier. Figure 5 shows the results of E_{excess} for different temperatures and concentrations. Clearly, it is evident that the nucleation barrier decreases with decreasing temperature and increasing average Cr concentration. The nucleation barrier becomes zero when Cr concentration approaches the spinodal concentration c_0=0.20, which is in agreement with spinodal decomposition theory. The maximum Cr concentrations of the nuclei corresponding to **Error! Reference source not found.**(a) are plotted in **Error! Reference source not found.**(b). Both the nucleation barrier and the maximum value of a critical nucleus strongly depend on the temperature and Cr concentration. These thermodynamic properties are important to calculate the nucleation rates and introduce the correct critical nuclei in PF modeling of precipitation kinetics.

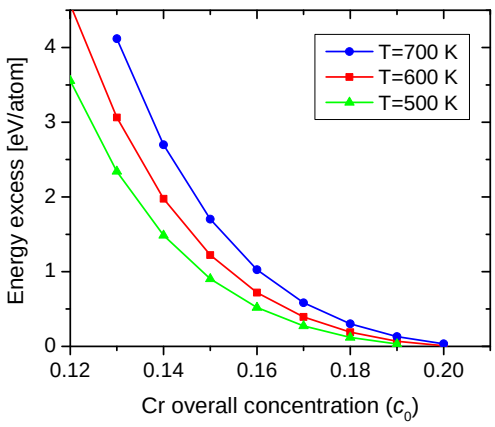

(a)

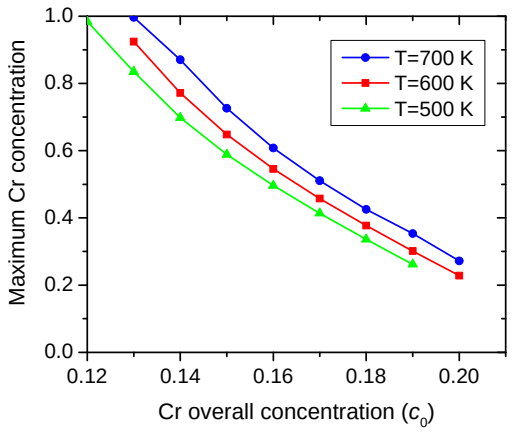

(b)

Figure 5. (a) The energy excess (nucleation barrier) required for the formation of a critical nucleus and (b) the maximum concentrations inside the critical nuclei at different temperatures and different overall Cr concentrations.

2.4 Growth kinetics of classical and non-classical nuclei

In classical nucleation theory, the concentration inside the critical nucleus is assumed to be $C_{Cr}^{P,eq}$, the equilibrium concentration of the precipitate phase. However, as shown in the preceding section, the concentration in a non-classical critical nucleus is much less than the equilibrium concentration. Thus, the question is, how do critical concentration profiles affect their growth kinetics? To answer, the growth kinetics of the critical nuclei with classical and non-classical concentration profiles is simulated with the PF model. In the simulations, we first numerically determine the critical concentration profile of a classical nucleus by examining the growth and shrinkage of different nuclei with a Cr concentration of $C_{Cr}^{P,eq}$ inside the nucleus and a smooth interface between the matrix and nucleus. Figure 6(a) shows the concentration profile of the classical critical nucleus for a given Cr overall concentration c_0=0.16 at temperature T=500 K. For comparison, the concentration profile of the non-classical critical nucleus from the CSDD method appears in the same figure. This shows that the classical and non-classical nuclei have quite different concentration profiles. In analyzing the evolution of the classical nucleus, it is interesting to find that the nucleus first shrinks to a critical state, then grows. Figure 6(b) depicts the evolution of the classical nucleus at the shrinkage stage, while the concentration profile of the nucleus at the critical state is plotted in Figure 6(c). For comparison, the non-classical critical nucleus predicted from the CSDD method is plotted in the same figure, showing that the concentration profile at the critical state is nearly the same as the non-classical nucleus. Figure 6(d) illustrates the temporal evolution at the growth stage. The result, showing that the classical nucleus concentration profile first evolves to the non-classical nucleus concentration profile, further proves the CSDD method's capability in searching for critical nuclei.

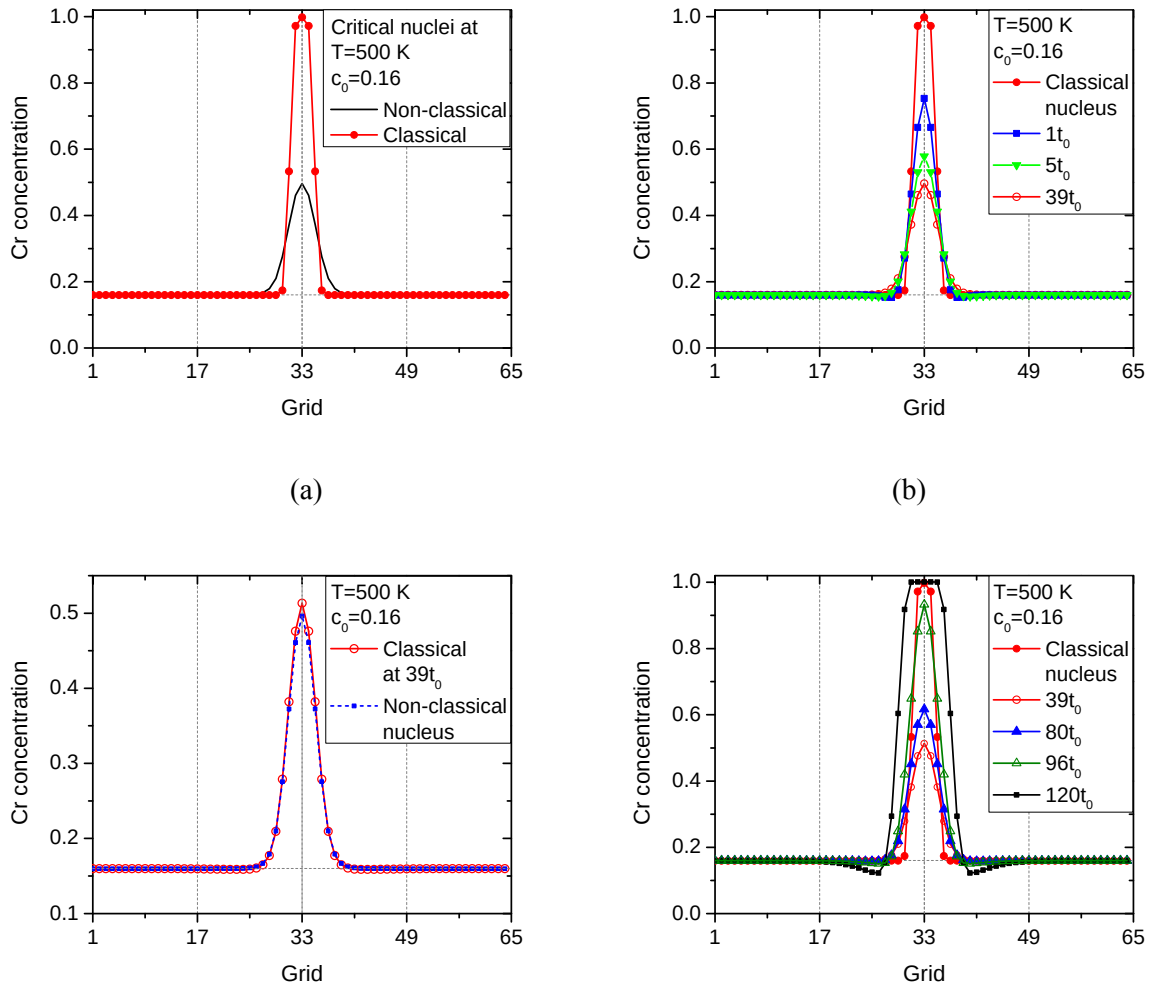

Figure 6. Classical nucleus profile of T=500 K and c_0=0.16 and its evolution growth with time. (a) Comparison of critical nucleus profiles between the classical nucleus and non-classical nucleus. (b) Nucleus evolution at its shrinking stage. (c) Comparison of the non-classical nucleus and classical nucleus at the stage with lowest concentration at its center. (d) Nucleus evolution at its growth stage.

The evolution kinetics of classical and non-classical nuclei is compared. Figure 7(a) shows the comparison of Cr concentration distribution evolution. Because the maximum concentration varies with time, the radius of the nucleus cannot reflect the growth kinetics. We analyze the evolution of the total Cr contents in Cr precipitates, which are plotted in Figure 7(b). Both Figure 7(a) and Figure 7(b) illustrate that the classical nucleus grows faster at the early growth stage than the non-classical nucleus. By examining the total amounts of Cr in the classical and non-

classical nuclei in Figure 6(a), we easily find that the difference in their growth kinetics attributes: 1) the classical critical nucleus requires more Cr than the non-classical one, and 2) when the classical nucleus shrinks to the critical state, the extra Cr causes a higher supersaturation around the nucleus compared to the non-classical one. If we compare the similarity of the two curves in Figure 7(b), we find that non-classical nucleus growth has a certain time delay. In classical nucleation theory, the diffusion-controlled growth of a spatial particle can be described by $R = \lambda(Dt)^{1/2}$, where R is the radius of the particle, D is the diffusivity, t is time, and λ is a dimensionless growth parameter that depends on the supersaturation, as well as the particle size.[22] It is clear that non-classical nucleus growth does not follow the growth kinetics of classical diffusion-controlled growth. The non-classical nucleus has a very long waiting time, which cannot be ignored when compared with the whole particle growth process. During this waiting time, the system almost does not evolve. Figure 7(c) and Figure 7(d) plot the evolution of the energy excess and maximum concentrations inside the nucleus and minimum concentration in the matrix. It is evident that the energy excess, as well as the maximum and minimum concentrations, changes very slowly during the waiting time. One explanation could be that the non-classical critical nuclei are at the saddle point of the energy landscape, where the driving force to grow is limited. After the long waiting time, nucleus growth speeds up. The energy excess starts deeply decreasing. The maximum concentration increases, and the minimum concentration decreases. Figure 7(d) shows how they gradually reach their thermal equilibrium concentrations. Afterward, the nucleus growth follows diffusion-controlled growth. The growth kinetics of the classical nucleus is different from that of the non-classical nucleus. The big differences are 1) the nucleus first shrinks, and 2) it has a shorter waiting time due to higher supersaturation around the nucleus. The results demonstrate that the non-classical nucleus at the early growth stage has a different growth kinetics from that predicted by the classical diffusion controlled growth theory. The deviation of the nucleus concentration profiles introduced in a PF model related to the critical nucleus concentration profile could result in a profound effect on the growth kinetics. Therefore, to correctly capture the kinetics of precipitation, it is essential to introduce the correct critical nuclei.

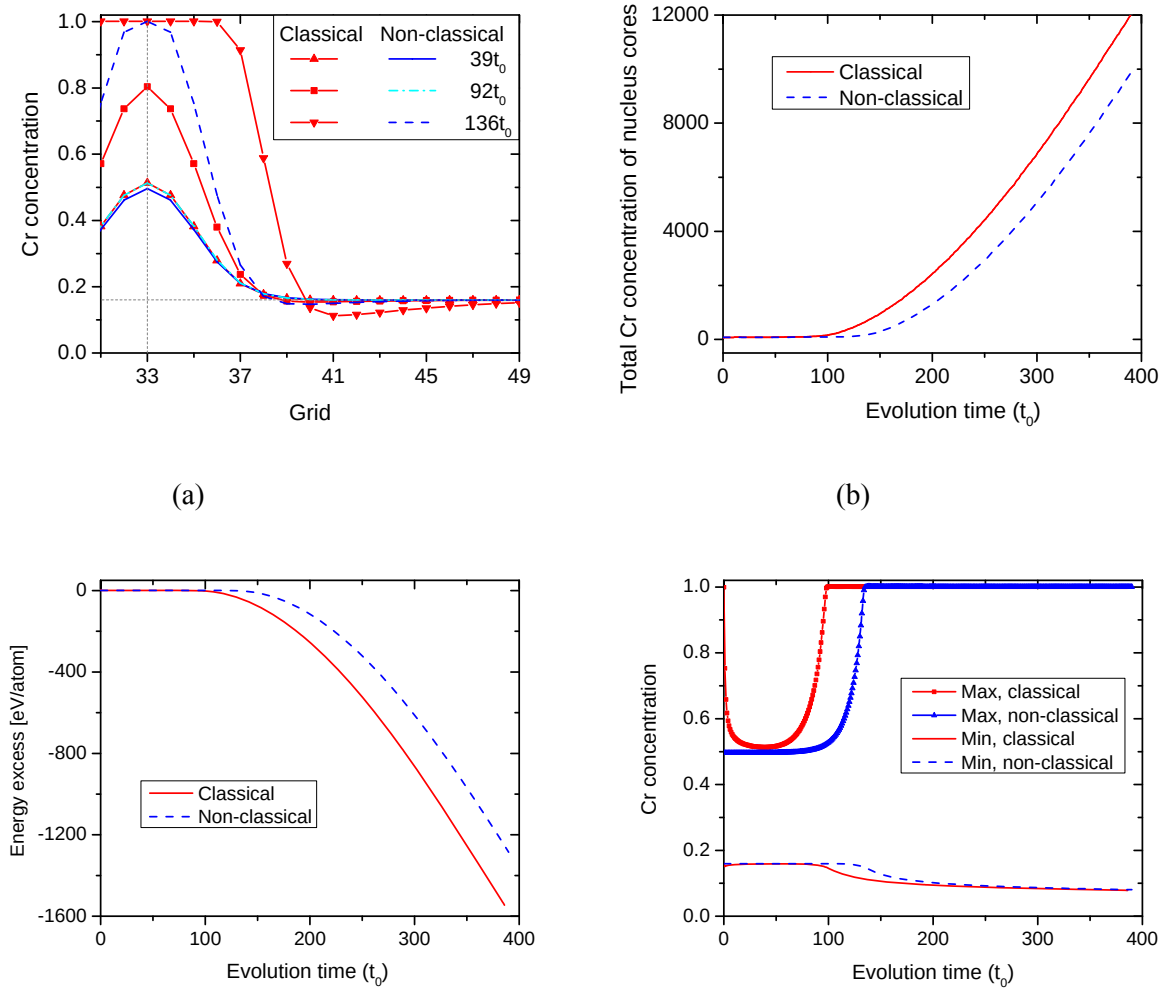

Figure 7. Comparison of the growth kinetics of the non-classical nucleus and classical nucleus. (a) Nucleus profile evolution with time. The dashed and solid lines represent the evolution of the non-classical nucleus. The lines with symbols represent the evolution of the classical nucleus. Only partial profiles are shown for clarity. Grid point 33 is the center of the spherical nuclei. (b) Total Cr concentration inside the nucleus cores. The core is defined as $C_{Cr} \geq 0.20$. The total Cr concentration in the simulation cell is 64×64×64×0.16=41943. (c) Evolution of the energy excess, and (d) the evolution of maximum concentration inside the nucleus and minimum concentration in the matrix.

2.5 Summary

With the thermodynamic and kinetic properties of Fe-Cr alloys from CALculation of PHAse Diagrams, or CALPHAD, calculations and atomistic simulations, the CSDD and PF method have been used to predict quantitatively the critical nucleus concentration profiles, nucleation energy barriers, and growth kinetics of Cr precipitates in Fe-Cr alloys. We have found that the critical nuclei of Cr precipitates from the CSDD method are non-classical because the concentration inside the nuclei is much smaller than the thermal equilibrium concentration calculated from the equilibrium phase diagram. The results are in agreement with atomic probe observations. Moreover, the simulations of critical nucleus evolution show a number of interesting phenomena: 1) a critical classical nucleus first shrinks to a non-classical nucleus, then grows; 2) a non-classical nucleus has much slower growth kinetics at the earlier growth stage compared to diffusion-controlled growth kinetics; and 3) a critical classical nucleus grows faster at the earlier growth stage than the non-classical nucleus. All of these results demonstrate it is critical to introduce the correct critical nuclei to correctly capture the kinetics of precipitation.

3. Implementation of the phase field model in MARMOT

3.1 Phase field modeling

In Fe-Cr alloys, the precipitates and matrix phases have the same bcc structure. One concentration can uniquely describe the precipitation. However, in most alloys, the precipitate phase has a different concentration and crystal structure. For example, Cu precipitates in Fe-Cu alloys have an fcc crystal structure, while the matrix phase, i.e., the Fe-Cu solid solution, has a bcc structure at low temperatures. In thermodynamic calculations such as CALPHAD, two free energy functions are needed to describe the free energies of the bcc matrix phase and the fcc precipitate phase. To describe the precipitation in such alloys, the PF model usually requires two field variables. One is the concentration, and the other is an order parameter that describes the different crystal structures. The total system free energy is described in a function of the concentration and order parameter. The WBM[23] and KKS models[24] are commonly used to describe the total free energy of the system.

The WBM and KKS models have yet to be implemented into MARMOT. In this section, we present the two models and implement them into MARMOT. The Fe-Cu alloys—important structure materials in nuclear reactors—are used as model alloys to present and test the models.

PF variables $c(\mathbf{r},t)$ and $\phi(\mathbf{r},t)$ are used to describe the concentration of Cu and the crystal structure, respectively. The total energy of the system is written as:

$$E = \int_V \left[f(c,\phi) + \frac{\kappa_c}{2}|\nabla c|^2 + \frac{\kappa_\phi}{2}|\nabla \phi|^2 \right] dV \,, \tag{16}$$

where $\mathbf{r}$ is the spatial coordinate, t is time, and V is the system volume. κ_c and κ_ϕ are the gradient energy coefficients. $f(c, \phi)$ defines the local free energy density. The evolution of the variables is described using:

$$\frac{\partial c}{\partial t} = \nabla \cdot \left\{ M \nabla \left(\frac{\delta E}{\delta c} \right) \right\} = \nabla \cdot \left\{ M \nabla \left(\frac{\partial f}{\partial c} - \kappa_c \nabla^2 c \right) \right\}, \tag{17}$$

$$\frac{\partial \phi}{\partial t} = -L \frac{\delta E}{\delta \phi} = -L \left(\frac{\partial f}{\partial \phi} - \kappa_\phi \nabla^2 \phi \right). \tag{18}$$

Equations (17) and (18) are the Cahn-Hilliard and Allen-Cahn equations, respectively. The local free energy $f(c, \phi)$ in both the WBM and KKS models is expressed as:

$$f(c,\phi) = [1 - \eta(\phi)] f_1(c_1) + \eta(\phi) f_2(c_2) + w g(\phi) \tag{19}$$

with

$$\eta(\phi) = \phi^2 (3 - 2\phi), \tag{20}$$

$$g(\phi) = \phi^2 (1 - \phi)^2 , \tag{21}$$

where $f_1(c_1)$ and $f_2(c_2)$ are the free energies of the matrix and precipitate phases, respectively. And, c_1 and c_2 are Cu concentrations in the matrix and precipitate phases, respectively. They can be obtained from thermodynamic calculations, such as CALPHAD. $\eta(\phi)$ is a shape function that describes the volume fraction of the precipitate phase at point **r.** $g(\phi)$ is the double well potential, and w is the height of the double well. The WBM model assumes the material is a mixture of the two phases with the same concentration, i.e., c_1=c_2=c. Thus,

$$\frac{\partial f}{\partial c} = [1 - \eta(\phi)] \frac{\partial}{\partial c} f_1(c) + \eta(\phi) \frac{\partial}{\partial c} f_2(c), \tag{22}$$

$$\frac{\partial f}{\partial \phi} = [- f_1(c) + f_2(c)] \eta'(\phi) + w g'(\phi). \tag{23}$$

Kim et al.[24] modify the WBM model by assuming the material is a mixture of the two phases that have the same chemical potential. This means the concentration and order parameter should satisfy the following equations:

$$c = [1-\eta(\phi)]c_1 + \eta(\phi)c_2\,, \tag{24}$$

$$\frac{\partial f_1(c_1)}{\partial c_1} = \frac{\partial f_2(c_2)}{\partial c_2}\,. \tag{25}$$

Then $\partial f / \partial c$ and $\partial f / \partial \phi$ in Eqs. (17) and (18) can be calculated by:

$$\frac{\partial f}{\partial c} = \frac{\partial}{\partial c_1} f_1(c_1, T) = \frac{\partial}{\partial c_2} f_2(c_2, T), \tag{26}$$

$$\frac{\partial f}{\partial \phi} = \eta'(\phi)\left\{[f_2(c_2) - f_1(c_1)] + (c_1 - c_2)\frac{\partial}{\partial c_1} f_1(c_1)\right\} + wg'(\phi). \tag{27}$$

Both the WBM and KKS models have been extensively used in modeling precipitations. In the following section, we implement them into MARMOT.

3.2 Implementation into MARMOT

The splitting scheme is used to solve the Cahn-Hilliard equation with the MARMOT framework. The chemical potential is calculated as:

$$\mu = \left(\frac{\partial f}{\partial c} - \kappa_c \nabla^2 c\right). \tag{28}$$

Then, the Cahn-Hilliard equation changes into:

$$\frac{\partial c}{\partial t} = \nabla \cdot \{M \nabla \mu\}\,. \tag{29}$$

Its weak form is:

$$\left(\frac{\partial c}{\partial t}, \xi\right) = (\nabla \cdot \{M\nabla\mu\},\ \xi) = -(M\nabla\mu, \nabla\xi) + \langle \xi, M\nabla\mu \cdot \mathbf{n}\rangle\,, \tag{30}$$

where the parentheses and angle brackets refer to interior and boundary integrals, respectively. ξ is a test function or weight function. The corresponding kernels are listed with underlines and can be found in the MARMOT library:

$$\underbrace{\left(\frac{\partial c}{\partial t},\xi\right)}_{\text{TimeDerivative}} = \underbrace{-\left(M\nabla\mu,\nabla\xi\right)}_{\text{SplitCHWRes}} + \left\langle M\nabla\mu\cdot\mathbf{n},\xi\right\rangle. \tag{318}$$

Similarly, we have a weak form of Eq. (25):

$$\left(\mu,\psi\right) = \left(\frac{\partial f}{\partial c},\psi\right) - \left(\kappa_c\nabla^2 c,\psi\right) = \left(\frac{\partial f}{\partial c},\psi\right) + \left(\kappa_c\nabla c,\nabla\psi\right) - \left\langle\kappa_c\nabla c\cdot\mathbf{n},\psi\right\rangle, \tag{32}$$

when κ_c is a constant. The corresponding kernels are listed as:

$$\underbrace{-\left(\mu,\psi\right)+\left(\kappa_c\nabla c,\nabla\psi\right)}_{\text{SplitCHRes}} + \underbrace{\left(\frac{\partial f}{\partial c},\psi\right)}_{\text{SplitCHBase}} - \left\langle\kappa_c\nabla c\cdot\mathbf{n},\psi\right\rangle = 0. \tag{33}$$

The weak form of the Allen-Cahn Eq. (18) is:

$$\left(\frac{\partial\phi}{\partial t},\zeta\right) = -\left(L\frac{\partial f}{\partial\phi},\zeta\right) + \left(L\kappa_\phi\nabla^2\phi,\zeta\right) = -\left(L\frac{\partial f}{\partial\phi},\zeta\right) - \left(L\kappa_\phi\nabla\phi,\nabla\zeta\right) + \left\langle L\kappa_\phi\nabla\phi\cdot\mathbf{n},\zeta\right\rangle, \tag{34}$$

when L and κ_ϕ are constants. The corresponding kernels are:

$$\underbrace{\left(\frac{\partial\phi}{\partial t},\zeta\right)}_{\text{TimeDerivative}} = \underbrace{-\left(L\frac{\partial f}{\partial\phi},\zeta\right)}_{\text{ACBulk}} \underbrace{-\left(L\kappa_\phi\nabla\phi,\nabla\zeta\right)}_{\text{ACInterface}} + \left\langle L\kappa_\phi\nabla\phi\cdot\mathbf{n},\zeta\right\rangle. \tag{35}$$

In the preceding equations, ψ and ζ also are test functions. $\left\langle M\nabla\mu\cdot\mathbf{n},\xi\right\rangle$, $\left\langle\kappa_c\nabla c\cdot\mathbf{n},\psi\right\rangle$, and $\left\langle L\kappa_\phi\nabla\phi\cdot\mathbf{n},\zeta\right\rangle$ are all the weak form of Neumann boundary conditions. So these boundary integrals do not appear when we consider periodic boundary conditions.

To implement the WBM and KKS models into MARMOT, the two kernels of $\left(L\frac{\partial f}{\partial\phi},\zeta\right)$ and $\left(\frac{\partial f}{\partial c},\psi\right)$ must be changed.

3.3 Application of WBM and KKS models in Fe-Cu alloys

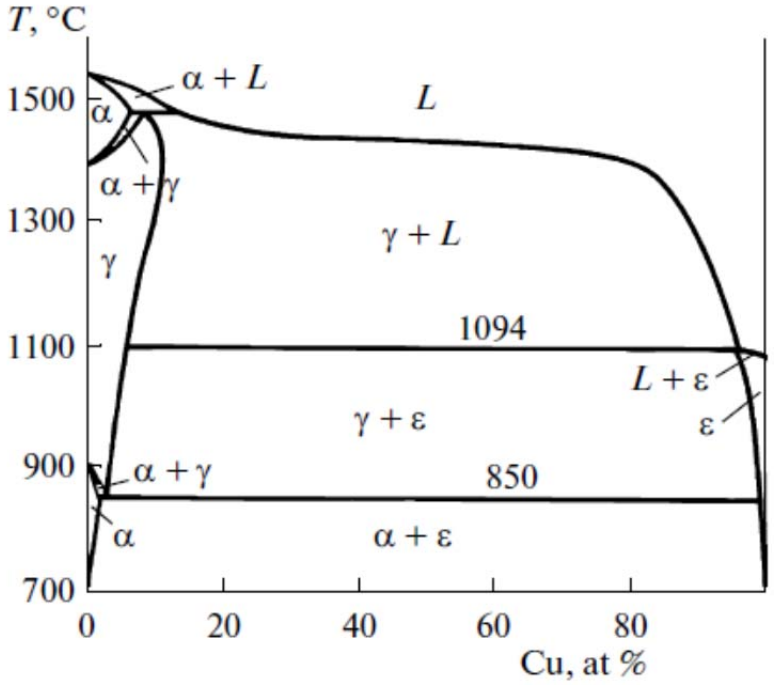

Figure 8. Equilibrium phase diagram of Fe-Cu alloys.[25]

Figure 8 provides the equilibrium phase diagram of Fe-Cu alloys, where α and γ indicate the bcc and fcc Fe-Cu solid solution and the ε phase is the fcc pure Cu. The free energy densities (f_1 and f_2) and their first derivatives of α-phase and γ-phase at different temperatures are plotted in Figure 9 and Figure 10, respectively, which are calculated with the Gibbs energy function provided in Refs. (7, 26). In the figures, R is the gas constant, and T is temperature.

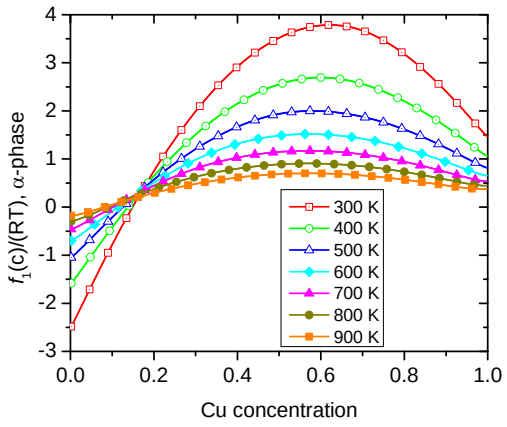

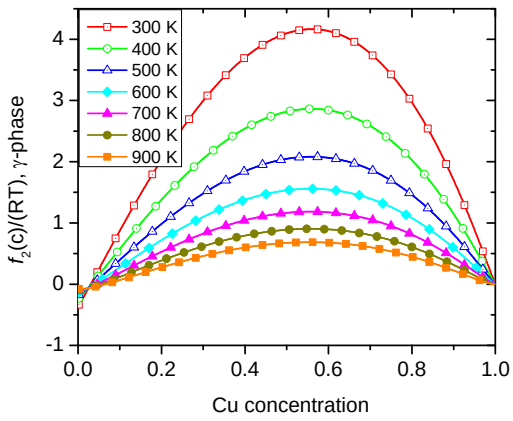

Figure 9. Free energy densities of α-phase (bcc) and γ-phase (fcc) in Fe-Cu alloys at different temperatures.

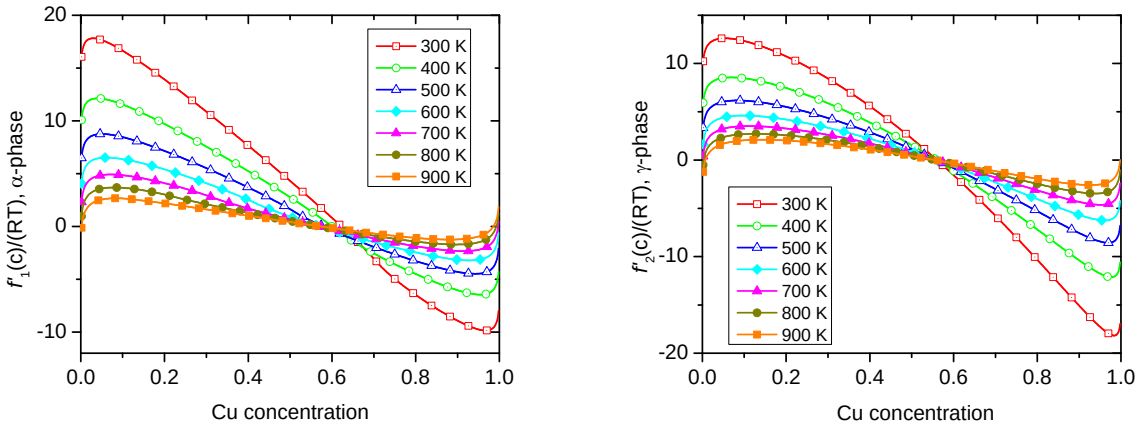

Figure 10. Derivatives of the free energy densities of α-phase (bcc) and γ-phase (fcc) in Fe-Cu alloys at different temperatures.

The equilibrium concentrations of Cu at the α-phase solid solution and γ-phase Cu precipitates (i.e., the ε-phase) can be obtained by determining their common tangent (listed in Table IV).

Table IV. Equilibrium concentrations of Cu at the α-phase solid solution and ε-phase Cu precipitates.

Temperature (K)	α-phase	ε-phase
400	3.95384e-7	1.
500	8.49763e-6	0.999999
563	0.000034038	0.999995
600	0.0000675729	0.999986
700	0.000308429	0.999891
773	0.000752067	0.99965
800	0.00101208	0.999489
900	0.00273375	0.998301

To simulate fcc Cu precipitate growth at given temperatures and concentrations, we use both the WBM and KKS models. The total free energy of the system is calculated with Eq. (16). The normalized evolution equations are:

$$\frac{\partial c}{\partial t^*} = \nabla^* \cdot \left\{ \nabla^* \left(\frac{\partial f^*}{\partial c} - \kappa_c^* \nabla^{*2} c \right) \right\} \tag{36}$$

$$\frac{\partial \phi}{\partial t^*} = -L^* \left(\frac{\partial f^*}{\partial \phi} - \kappa_\phi^* \nabla^{*2} \phi \right), \tag{37}$$

where $\kappa_c^* = \frac{\kappa_c}{RT_{ref} l_0^2}$, $\kappa_\phi^* = \frac{\kappa_\phi}{RT_{ref} l_0^2}$, $f^* = \frac{f}{RT_{ref}}$, $t^* = \frac{tDc_0(1-c_0)T_{ref}}{Tl_0^2}$, and $L^* = \frac{LRTl_0^2}{Dc_0(1-c_0)}$ with the assumption of $M = Dc(1-c)/(RT) \cong Dc_0(1-c_0)/(RT)$. Table V lists the material properties and normalized model parameters. The model parameters (κ_c, κ_ϕ, w) are determined numerically by the interfacial properties: interface thickness and interfacial energy. An interfacial energy of 1J/m^2 is assumed. For the KKS model, the solution of nonlinear equations (Eqs. 24-25) is found by searching the pre-prepared table of Eq. (25).

Table V. Parameters used in the simulations.

Parameter	WBM model	KKS model
Aging temperature (K)	773, 563	773, 563
Gradient energy coefficients (Jm^2/mol)	κ_c=5.0e-15 κ_ϕ=2.0e-15(1D)	κ_c=0.0 κ_ϕ=10.e-15(1D)
Parameter w (J/mol)	1.0e4	1.0e5
Diffusion coefficient[27] $D = D_0 \exp[-Q/(RT)]$		
D_0 (m^{2}s^{-1})	4.7e-5	4.7e-5
Q (J/mol)	2.44e5	2.44e5
Characteristic length l_0 (m)	0.296e-9	0.296e-9
L^*	1.0	1.0
Δt^*	1.e-4 (T=773K), e-5 (T=563K)	1.0e-3
Molar volume V_m (m^3/mol)[27]	7.09e-6	7.09e-6

3.4 Results and discussion

To examine both the WBM and KKS models, we simulate the growth kinetics of fcc Cu precipitate (i.e., the ε-phase) in 1-D and two-dimensional (2-D) cases. Table V lists the parameters used. Figure 11 and Figure 12 present the growth kinetics of a same-sized fcc Cu precipitate in 1-D case for different temperatures (773 K and 563K) and different initial concentrations (c_0=0.013 and 0.05) in the Fe-Cu bcc solid solution phase. The curves with open circles are obtained from the KKS model, while the curves with open diamonds are from the WBM model. We can clearly observe that both models produce almost the same growth kinetics. Because the two models use the same thermodynamic and kinetic properties, including the free energies and interfacial energies, the small difference in the growth kinetics should be from the different assumptions of the two models at the interface. In the simulations, we determine that the KKS model can use a larger time step (Δt^*) than the WBM model. Furthermore, the time step in the KKS model is almost temperature independent, while the time step decreases with a temperature decrease. Therefore, the KKS model has much better computational efficiency than the WBM model. Regarding the effect of Cu concentration on growth kinetics, the precipitate grows faster in a system with higher Cu concentration than one with lower Cu concentration, as expected.

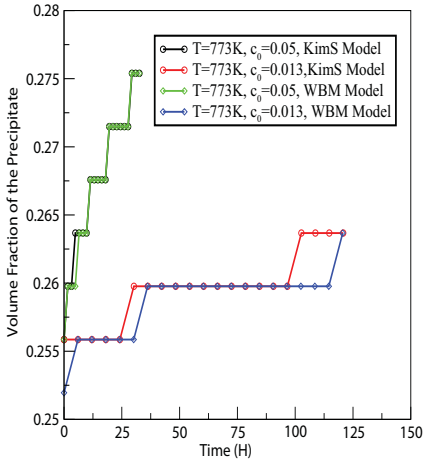

Figure 11. Fcc Cu precipitate volume fraction change with time in a 1-D simulation cell simulated by both the WBM and KKS models under 773 K and different Cu initial concentration c_0.

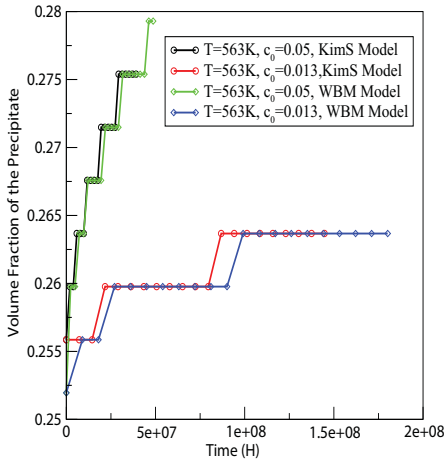

Figure 12. . Fcc Cu precipitate volume fraction change with time in a 1-D simulation cell simulated by both the WBM and KKS models under 563 K and different Cu initial concentration c_0.

We also compare the growth kinetics of fcc Cu precipitate in a 2-D case, and Figure 13 showcases the results. These results support the same conclusions: the WBM and KKS models produce the same results, and the KKS model has higher numerical efficiency than the WBM model.

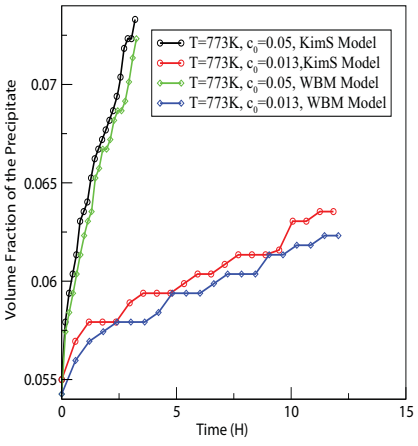

Figure 13. Fcc Cu precipitate volume fraction change with time in a 2-D simulation cell simulated by both the WBM and KKS models under 773 K and different Cu initial concentration c_0.

In summary, two PF models—WBM and KKS—have been used for simulating the growth kinetics of fcc Cu precipitates in bcc Fe-Cu alloys. Both models have been implemented into MARMOT and within Fast Fourier Transition (FFT). With FFT codes, the model parameters and growth kinetics in 1-D and 2-D simulation cells have been evaluated. The results demonstrate that both models produce the same growth kinetics, but the KKS model has better performance in terms of numerical efficiency. Currently, 3-D simulations of the KKS models are underway. At the time when this report is written, the implementation in MARMOT codes can successfully compile. Since the thermodynamic models directly obtained from CALPHAD involve heavy natural log functions, we are still testing the MARMOT code in terms of numerical convergence and accuracy in the solution process. We are also considering using the tabulated chemical potentials to avoid the calculation of natural log, which can greatly improve the numerical stability and efficiency from our numerical results of FFT codes.

4. Conclusion

In this report, we summarize our effort in 1) developing a method to predict the thermodynamic properties of critical nuclei and 2) implementing the WBM and KKS models, which simultaneously solve the concentration and order parameter fields, into MARMOT. For given thermodynamic properties of the system, we are able to obtain the thermodynamic properties of classical and non-classical critical nuclei, i.e., the concentration profile of a critical nucleus and nucleation barrier. With this information, the nucleation rate can be calculated, and the nucleation process can be introduced into PF modeling. As noted, we also implement the WBM and KKS models into MARMOT, allowing for simulations of more complicated phase transitions that involve diffusion and structural changes. The simulations with FFT codes demonstrate that the KKS model is efficient in both length and time scales, enabling increases to the physical domain and time. The testing of MARMOT codes and the implementation of the nucleation process into MARMOT codes are ongoing.

Acknowledgments

The authors would like to thank Dr. M.R. Tonks for the great help during the implementation of WBM models into MARMOT. This research was supported by the U.S. Department of Energy's (DOE) Nuclear Energy Advanced Modeling and Simulation (NEAMS) Program at Pacific Northwest National Laboratory (PNNL). PNNL is operated by Battelle for the DOE under Contract No. DE-AC05-76RL01830.

References

[1] S. B. Biner, M. R. Tonks, P. C. Millett, Y. L. Li, S. Y. Hu, F. Gao, X. Sun, D. Schwen, E. Martinez, A. Caro, and D. Anderson, *Progress on Generic Phase Field Method Development*, PNNL Technical Report, PNNL-21811, Richland, Washington, 2012.
[2] G. Bonny, D. Terentyev, and L. Malerba, Comp. Mater. Sci. **42**, 107 (2008).
[3] S. Novy, P. Pareige, and C. Pareige, J. Nucl. Mater. **384**, 96 (2009).
[4] D. Gaston, C. Newman, G. Hansen, and D. Lebrun-Grandie, Nucl. Eng. Des. **239**, 1768 (2009).
[5] L. Q. Chen, Ann. Rev. Mater. Res. **32**, 113 (2002).
[6] M. R. Tonks, D. Gaston, P. C. Millett, D. Andrs, and P. Talbot, Comp. Mat. Sci. **51**, 20 (2012).
[7] J. Miettinen, CALPHAD **27**, 141 (2003).
[8] L. Zhang, L. Q. Chen, and Q. Du, Acta Mater **56**, 3568 (2008).
[9] R. L. Klueh and D. R. Harries, *High-Chromium Ferritic and Martensitic Steeels for Nuclear Applications*, ASTM International, MONO3, Bridgeport, New Jersey, 2001.
[10] P. J. Grobner, Metall. Trans. **4**, 251 (1973).
[11] J. N. Mohapatra, Y. Kamada, H. Kikuchi, S. Kobayashi, J. Echigoya, D. G. Park, and Y. M. Cheong, IEEE. Trans. Magn. **47**, 4356 (2011).
[12] P. Scott, J. Nucl. Mater. **211**, 101 (1994).
[13] L. Q. Chen and J. Shen, J. Comp. Phys. Comm. **108**, 147 (1998).
[14] D. Schwen, E. Martinez, and A. Caro, J. Nucl. Mater. **439**, 180 (2013).
[15] A. Caro, M. Caro, P. Klaver, B. Sadigh, E. M. Lopasso, and S. G. Srinivasan, JOM **59**, 52 (2007).
[16] B. Sadigh and P. Erhart, Phys. Rev. B **86**, 134204 (2012).
[17] L. Zhang, L. Q. Chen, and Q. Du, Phys. Rev. Lett. **98**, 265703 (2007).
[18] L. Zhang, L. Q. Chen, and Q. Du, Commun. Comput. Phys. **7**, 674 (2010).
[19] L. Zhang, L. Q. Chen, and Q. Du, J. Comput. Phys. **229**, 6574 (2010).
[20] J. Zhang and Q. Du, Siam J Numer Anal **50**, 1899 (2012).
[21] J. Zhang and Q. Du, J. Comput. Phys. **231**, 4745 (2012).
[22] P. E. J. Rivera-Diaz-del-Castillo and H. K. D. H. Bhadeshia, Mater. Sci. Technol. **17**, 30 (2001).
[23] A. A. Wheeler, W. J. Boettinger, and G. B. McFadden, Phys. Rev. A **45**, 7424 (1992).
[24] S. G. Kim, W. T. Kim, and T. Suzuki, Phys. Rev. E **60**, 7186 (1999).
[25] J. W. Christian, *The Theory of Transformations in Metals and Alloys, Part 1: Equilibrium and General Kinetic Theory*, Pergamon Press, Oxford, England, 1975.
[26] T. Koyama, K. Hashimoto, and H. Onodera, Mater. Trans. **47**, 2765 (2006).
[27] *Metals Data Book*, Japan Institute of Metals, Maruzen, Tokyo, Japan, 1993.